Thin Solid Films 668 (2018) 50–55

Contents lists available at ScienceDirect

Thin Solid Films

journal homepage: www.elsevier.com/locate/tsf

Suppression of B2 phase in Pd_zCu_{1-z} alloy thin films

Xiaoxiao Yu[a], Andrew J. Gellman[a,b,*]

[a] Dept. of Chemical Engineering, Carnegie Mellon University, Pittsburgh, PA 15213, USA
[b] W.E. Scott Institute for Energy Innovation, Carnegie Mellon University, Pittsburgh, PA 15213, USA

ARTICLE INFO

Keywords:
Palladium
Copper
Alloy
Phase transition
X-ray photoemission
Nanoscale
Core level shift

ABSTRACT

Thin films of pure metals and alloys can adopt phases that differ from those of the corresponding bulk alloy phase diagram. In the bulk, Pd_zCu_{1-z} adopts a B2 phase (CsCl structure) for $0.35 < z < 0.55$, in spite of the fact that pure Pd and Cu both have face centered cubic (FCC) bulk crystal structures. Herein, we demonstrate that this transition to the B2 phase is suppressed in thin film Pd_zCu_{1-z} alloys with thickness < 6 nm. Spatially resolved X-ray photoemission spectroscopy was used to map the Cu $2p_{3/2}$ core level shifts (CLS, $\Delta E_{CLS}^{Cu}(z)$) across a Pd_zCu_{1-z} composition spread alloy film (CSAF) as a function of both composition and film thickness. In the FCC phase, the Cu $2p_{3/2}$ binding energy decreases monotonically across the range $z = 0 \rightarrow 1$. At $T < 873$ K, there is an additional discontinuous CLS over the composition range of the B2 phase, $0.35 < z < 0.55$. Thus, the Cu $2p_{3/2}$ CLS can be used to distinguish between the B2 and FCC phases. After annealing the Pd_zCu_{1-z} CSAF to 700 K, the bulk B2 phase was observed at film thicknesses > 6 nm. However, at film thicknesses in the range 4–6 nm, only the FCC phase was observed. Stabilization of the FCC phase for films that are < 6 nm thick may be due, in part, to surface energy effects.

1. Introduction

Multicomponent alloy nanomaterials have potential utility in many fields (e.g. catalysis, sensing, optics, membranes and sorbents) [1–5]. One of the most exciting characteristics of multicomponent alloy nanoparticles is that they can adopt phases that are different from those of the bulk alloy at the same composition. For instance, bimetallic mixtures of AgNi, AgPt and AuPt, have broad composition ranges over which they are immiscible in the bulk; however they form solid solutions at the nanoscale regime [6–9]. The same phenomenon can be observed in alloy thin films. Herein, we refer to these as dimensionally stabilized phases, wherein alloy phases, A_zB_{1-z}, in nanoscale morphologies are determined by both composition, z, and dimension, d. These dimensionally stabilized alloy phases can serve as the basis for design of materials with properties that could not be predicted or obtained from bulk alloys. The experimental approach to determining the phase behavior of materials across composition and size space, (z, d), can be time-consuming, requiring the preparation and characterization of a large set of samples with discrete size and composition. Herein, we use Composition Spread Alloy Films (CSAFs) having a composition spread in one direction and a thickness gradient in another to identify a new dimensionally stabilized phase of the Cu_zPd_{1-z} binary alloy.

Comprehensive study of the properties of nanoscale alloy materials can be accelerated by use of high-throughput methods based on materials libraries that span both size and composition space. High-throughput methods have evolved rapidly over the past decade, allowing a systematic approach to preparation, characterization, and measurement of functional properties on different types of materials libraries in a rapid and efficient fashion [10–14]. CSAFs are materials libraries based on thin alloy films that have lateral composition gradients allowing one to create all possible compositions of a binary alloy (A_zB_{1-z}, $z = 0 \rightarrow 1$) or ternary alloy ($A_zB_yC_{1-z-y}$, $z = 0 \rightarrow 1$ and $y = 0 \rightarrow 1-z$) in a single film. Over the past decade, CSAFs have been used frequently as libraries for high-throughput studies of alloy properties [15–17]. In this work, we use a variant on the CSAF which spans both alloy composition and film thickness, in order to study alloy nanomaterials. Fig. 1 illustrates a binary A_zB_{1-z} CSAF with a composition gradient in the vertical direction and a linear thickness gradient, d, in the horizontal direction. This CSAF can be used to map Cu_zPd_{1-z} alloy properties across (z, d) space with arbitrarily high resolution.

1.1. Pd_zCu_{1-z} bulk phase diagram

Palladium is widely used for catalysts, electrodes, sorbents, and membranes. Palladium is employed in membranes for separation or purification of hydrogen [18], as well as in sorbents for warm gas clean-

* Corresponding author at: Dept. of Chemical Engineering, Carnegie Mellon University, Pittsburgh, PA 15213, USA.
E-mail address: gellman@cmu.edu (A.J. Gellman).

https://doi.org/10.1016/j.tsf.2018.10.018
Received 21 June 2018; Received in revised form 21 September 2018; Accepted 10 October 2018
Available online 12 October 2018
0040-6090/ © 2018 Elsevier B.V. All rights reserved.

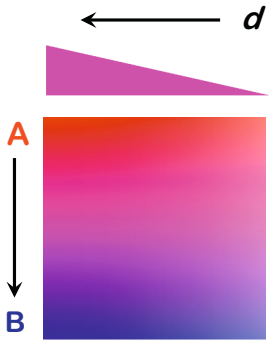

Fig. 1. Binary A_zB_{1-z} CSAF with a linear thickness, *d*, gradient in the horizontal direction and a composition, *z*, gradient along the vertical direction.

up of coal derived syngas [19–21]. In these applications, Pd is often alloyed with secondary components such as Cu and Ag to provide mechanical stability and sulfur tolerance during operation [22–29]. Both Pd and Cu have face centered cubic (FCC) bulk structures. However, at temperatures < 873 K, the Pd_zCu_{1-z} bulk phase diagram exhibits a B2 phase (ordered BCC lattice with Pd and Cu in a CsCl structure) across a broad composition range of $0.35 < z < 0.55$ [26,30]. This B2 phase impacts the performance of Pd_zCu_{1-z} alloy membranes used for hydrogen purification and in membrane reactors for hydrogenation catalysis. The bulk hydrogen permeance of Pd_zCu_{1-z} in the $0.35 < z < 0.55$ composition range is roughly an order of magnitude higher in the B2 phase than in the FCC phase [31]. If the formation of the B2 phases were suppressed in ultrathin Pd_zCu_{1-z} alloy membranes, this functional advantage would be lost [32]. It has also been shown that the rate of H_2 dissociation on the $Pd_{0.47}Cu_{0.53}$ surface is much higher on the surface of the FCC phase than on the B2 phase [33,34]. If the FCC phase can be stabilized in Pd_zCu_{1-z} alloy nanoparticles at $T < 873$ K, the performance of nanoparticulate Pd_zCu_{1-z} hydrogenation catalysts could be greatly improved over the activity of larger particles of the same composition.

Correlation of structure and function at the nanoscale requires phase determination in nanoscale morphologies. An experimental methodology based on the use of Cu $2p_{3/2}$ core level binding energies as measured using x-ray photoemission spectroscopy (XPS) has been developed recently for determining the phase behavior of Pd_zCu_{1-z} alloys [34,35]. This makes use of a high-throughput approach using spatially resolved XPS on a Pd_zCu_{1-z} CSAF to map the Cu $2p_{3/2}$ core level shifts (CLS) in binding energy relative to the $2p_{3/2}$ binding energy in pure Cu, $\Delta E_{CLS}{}^{Cu}(z) = E_{2p}{}^{Cu}(z) - E_{2p}{}^{Cu}(0)$. The CLS is sensitive to the alloy phase, exhibiting a discontinuous shift across the FCC-B2-FCC phase boundaries because these are order-disorder transitions [34]. Density functional theory calculations have shown that the Cu $2p_{3/2}$ binding energy is sensitive to the number of Cu atoms in the nearest neighbor shell of the Cu atom from which the electron is photoemitted. The Cu $2p_{3/2}$ binding energy shifts discontinuously across the phase boundary because the FCC phase is a random solid solution in which Cu atoms can be nearest neighbors while Cu atoms in the ordered B2 phase have no Cu atoms in their nearest neighbor shell. Thus, measurement of the Cu $2p_{3/2}$ CLS across $0.35 < z < 0.55$ can be used to distinguish between the ordered B2 phase and disordered FCC phase. One of the important advantages of using XPS for phase analysis is that it allows determination of the structure/phase of nanomaterials and in the near surface (1–2 nm) regions of bulk alloys; morphologies in which structure determination is not easy.

The work described herein uses Cu $2p_{3/2}$ CLS measurements to study the phases present in ultra-thin (< 8 nm) Cu_zPd_{1-z} CSAFs. In continuous films that are < 6 nm thick, the B2 phase disappears. This may be attributed, in part, to the fact that surface energy difference between the FCC and B2 phases acts to stabilize the FCC phase relative to the B2 phase once the film thickness drops to < 6 nm.

2. Experimental methods

2.1. Pd_zCu_{1-z} CSAF preparation

A rotatable shadow mask CSAF deposition tool developed in house was used for creation of the Pd_zCu_{1-z} CSAFs with both composition and thickness gradients [36]. The two pure components were deposited simultaneously from independent electron beam evaporators (Mantis Deposition, Inc.) directed at the $14 \times 14\ mm^2$ Mo substrate. Two independent shadow masks are positioned between the wide-aperture (5 mm diameter) e-beam sources and the substrate such that the flux from each source has a linear gradient across a ~7 mm wide band spanning the deposition substrate. The flux along one edge of the band is zero and increases to a maximum at the other edge of the band. The orientations of the rotatable shadow masks control the direction of the flux gradient from each source resulting a complex composition-thickness distribution across the substrate surface (Fig. 2).

The deposition substrate was a $14 \times 14 \times 2.5\ mm^3$ piece of

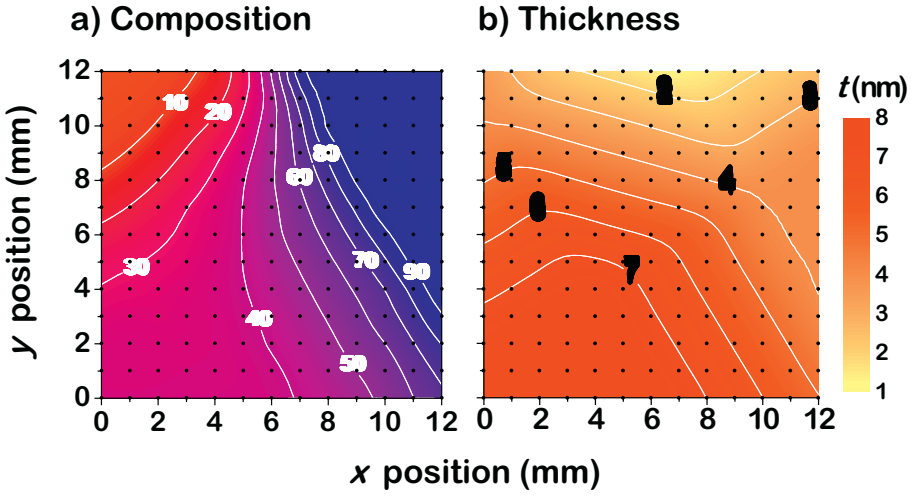

Fig. 2. a) Contour map of Pd composition, $z(x,y)$, across the Pd_zCu_{1-z} CSAF library, as measured using XPS at points on a 13 × 13 grid with 1 mm spacing. b) Thickness map, $d(x,y)$, across the Pd_zCu_{1-z} CSAF determined from EDX measurements of the thicknesses of Pd and Cu in the thickest regions combined with the known composition distribution obtained using XPS.

polycrystalline Mo substrate polished to a roughness of < 3 nm (Valley Design Corp). Mo was chosen to minimize interdiffusion between the CSAF components and the substrate during heating [26,37,38]. The substrate surface was sputter cleaned by a 2 kV Ar^+ beam with ~10 mA emission current for 20 min to remove any contaminants or oxide and then annealed at 700 K for 1 h in ultrahigh vacuum (UHV). The CSAF was deposited after the Mo substrate had cooled to room temperature under UHV conditions (~3×10^{-7} Pa). The deposition rate for each source was calibrated with a Maxtek quartz crystal microbalance to give a flux of ~0.2 nm per min. Deposition for 20 min generated a Pd_zCu_{1-z} CSAF with a thickness gradient from $d = 1 \rightarrow 8$ nm and a composition gradient from pure Cu to pure Pd, $z = 0 \rightarrow 1$. Note that the deposition geometry results in a composition-thickness map (Fig. 2) that is more complex than the orthogonal distribution implied by Fig. 1.

2.2. EDX characterization of thickness on Pd_zCu_{1-z} CSAF

After deposition, the Pd_zCu_{1-z} CSAF was transferred to a Tescan Vega 3 scanning electron microscope (SEM) with an Oxford Instruments X-mas 80 mm^2 detector for energy dispersive x-ray spectroscopy (EDX) analysis. The CSAF component concentration distribution was characterized by EDX spectra taken at 169 points on a 12 × 12 mm^2 grid of points spaced by 1 mm across an area centered on the 14 × 14 mm^2 Mo substrate. At each measurement point, the 11.24 keV SEM electron beam was rastered across a 50 × 50 μm^2 area to obtain an EDX spectrum over an x-ray energy of 0–10 keV. The thickness of the Pd_zCu_{1-z} alloy film was < 10 nm, but the EDX characterization depth is > 300 nm [39]. Assuming that the sampled volume consists of a homogenous Pd_zCu_{1-z} film on an infinitely thick Mo substrate, the INCA ThinFilmID software was used to quantify the concentrations of Pd, Cu, O, C and Mo at each analysis point and to determine the thickness of the Pd_zCu_{1-z} CSAF.

2.3. XPS mapping of composition and phase

The Pd_zCu_{1-z} CSAF library was transferred to a ThetaProbe® surface analysis system (ThermoFisher Scientific Inc.) for spatially resolved XPS measurements after heating to temperatures of 300, 600 and 700 K in a vacuum of ~10^{-7} Pa. Al K_α radiation (1486.6 eV) from a monochromated X-ray source was focused to a 200 μm diameter spot size and used to obtain XP spectra at 169 discrete points on a 12 × 12 mm^2 grid of points space by 1 mm and centered on the 14 × 14 mm^2 Pd_zCu_{1-z} CSAF. The XP spectra were collected across 10 eV binding energy ranges centered on the Cu $2p_{3/2}$, Pd $3d_{3/2}$ and Mo $3d_{5/2}$ peaks. The XP spectra were collected with an analyzer pass energy of 100 eV with a 0.1 eV step size and 0.1 s dwell time. The XPS peak area and position were determined by performing the Thermo "Smart" background subtraction and peaking fitting with a fixed 30% Lorentzian and 70% Gaussian shape using the Thermo Avantage Processing software. The atomic composition was calculated by applying Thermo sensitivity factors to the peak areas.

2.4. Composition distribution model and thickness gradient of Pd_zCu_{1-z} CSAF

A Composition Distribution Model (CDM) has been developed based on the deposition geometry of the RSM-CSAF deposition tool, and assuming that each alloy component is deposited as a wedge in real space starting from zero along one line across the substrate and increasing linearly to a maximum value along a parallel line [38]. After determining the thickness distribution parameters of the Pd and Cu wedges (zero-line orientation, wedge width and maximum molar thickness of each component) by fitting to the 169 XPS-measured compositions collected on the grid spanning a 12 × 12 mm^2, the composition and component thickness at all real space locations on the CSAF can be predicted using the CDM. The best-fit CDM was defined by the set of thickness distribution parameters for each component which minimized the difference between the CDM-predicted composition and XPS-measured composition for all 169 points measured on the surface of the Pd_zCu_{1-z} CSAF. The CDM then serves as the map for estimation of composition, z, and thickness, d, at all points on the CSAF.

3. Results

3.1. Composition and thickness map for Pd_zCu_{1-z} CSAF

A combination of XPS and EDX measurements was used to determine the composition map, $z(x,y)$ (Fig. 2a), and thickness map, $d(x,y)$ (Fig. 2b), across the physical dimensions of the Pd_zCu_{1-z} CSAF. The Pd and Cu compositions were measured at each point using the Pd $3d_{3/2}$ and Cu $2p_{3/2}$ XPS peaks. Prior work has shown that XPS provides a good estimate of the bulk composition of Pd_zCu_{1-z} CSAFs [16,26]. For each alloy component, i = Pd or Cu, the molar areal concentrations, c_i, at the thickest portions of the wedges were determined using EDX to be ${c_{Pd}}^{max} = 446 \pm 3$ μmol/m^2 and ${c_{Cu}}^{max} = 545 \pm 3$ μmol/m^2. The physical thicknesses of each component, d_i, at the thickest portions of the wedge were calculated to be ${d_{Pd}}^{max} = 3.95 \pm 0.03$ nm and ${d_{Cu}}^{max} = 3.87 \pm 0.02$ nm based on Eq. (1):

$$d_i = \frac{c_i \times M_i}{\rho_i} \quad (1)$$

where M_i and ρ_i are the molar masses and volumetric mass densities of each component, respectively. The maximum thicknesses, ${d_{Pd}}^{max}$ and ${d_{Cu}}^{max}$, and the composition map, $z(x,y)$, were then used to parameterize a concentration distribution model (CDM) which describes the physical distribution of each component across the CSAF as a wedge with a maximum thickness plateau at one edge and a linear decrease to a zero thickness at the other edge [38]. This is consistent with the expected distribution based on the film deposition method and with EDX-based composition measurements made on thicker CSAFs [26,36,38]. The map of Pd composition determined from the CDM is illustrated in Fig. 2a. The difference between the CDM predicted Pd compositions and those determined from XPS measurements ($\varepsilon_{Pd} = {z_{Pd}}^{CDM} - {z_{Pd}}^{XPS}$) is 1.1 ± 1.0 at.% where the uncertainty represents one standard deviation. The error arising from the surface segregation after annealing at 700 K is within 1.5 at.% of the bulk composition over the entire composition range of the Pd_zCu_{1-z} CSAF [26]. The thickness maps for each alloy component can be determined from Eq. (1) using the concentrations predicted from the CDM as shown in Fig. 2a. Fig. 2b illustrates the map of total film thickness, $d(x,y)$, spanning the range 1.3 to 7.8 nm.

3.2. Pd_zCu_{1-z} film dewetting from Mo substrate

After the composition and thickness of the Pd_zCu_{1-z} CSAF were characterized at room temperature, it was annealed at 600 K and 700 K for 30 mins. For CSAFs that are ~100 nm thick, annealing at temperatures in this range is sufficient to achieve crystalline films that have phases identical to those of the bulk phase diagram [26,34]. This annealing does not cause dewetting of Pd_zCu_{1-z} films with thickness $d \approx 100$ nm. However, over-annealing of thinner films can result in dewetting from the substrate, driven by lowering of the total free energy of the surfaces and interfaces of the film and substrate [40]. Dewetting of thinner films occurs at lower temperatures and shorter times than dewetting of thick films. These issues limit the temperatures at which the CSAFs can be used.

Dewetting of Pd_zCu_{1-z} CSAFs is detected by the appearance of the substrate Mo $3d_{5/2}$ XPS signals after annealing. The evidence for Pd_zCu_{1-z} film dewetting from the Mo substrate is provided in Fig. 3a, where the Mo $3d_{5/2}$ peak area is plotted as a function of initial film thickness as deposited at 300 K, and after annealing at 600 K and 700 K for 30 mins. The Mo $3d_{5/2}$ XP spectra (binding energy = 227.9 eV) collected from a point with an initial film thickness of 2.5 nm are

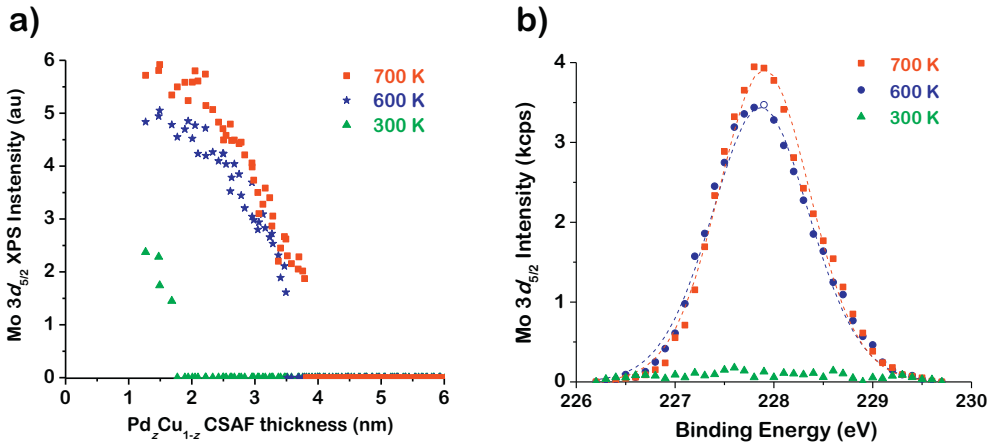

Fig. 3. a) Mo $3d_{5/2}$ peak area measured as a function of CSAF thickness and b) background-subtracted Mo $3d_{5/2}$ peak spectra at a film thickness of 2.5 nm at 300 K, and after annealing for 30 mins at 600 K, and 700 K. The discontinuous increases in Mo $3d_{5/2}$ peak area at 3.5 and 3.8 nm after heating to 600 and 700 K, are clear evidence of CSAF dewetting from the Mo substrate.

illustrated in Fig. 3b. Fig. 3a shows that no Mo $3d_{5/2}$ signal was observed at initial Pd_zCu_{1-z} CSAF thicknesses > 1.7 nm as deposited at 300 K. After annealing at 600 K for 30 min there is a discontinuous appearance of the Mo $3d_{5/2}$ signal at an initial CSAF thickness of 3.5 nm, followed by an increase in the signal with decreasing initial thickness. After annealing at 700 K for 30 min, the onset of Mo $3d_{5/2}$ signal occurs at an initial thickness of 3.8 nm and the Mo $3d_{5/2}$ signal at $d < 3.5$ nm increases by ~20% over its intensity following the 600 K anneal. These data provide clear evidence of CSAF dewetting as a result of annealing, but only at films with initial thicknesses $d \leq 4$ nm.

Further evidence of CSAF dewetting in regions with an initial thickness < 4 nm is revealed by SEM images obtained after annealing at 700 K for 30 min (Fig. 4). These were obtained from regions of the CSAF with similar compositions, $Pd_{0.45}Cu_{0.55}$ and $Pd_{0.48}Cu_{0.52}$, but initial thicknesses of $d = 2.2$ and 5.2 nm. The micrograph of the 2.2 nm film in Fig. 4a reveals contrast variation across the image whereas, the image of the thicker 5.2 nm film in Fig. 4b reveals virtually no contrast. Coupled with the appearance of the Mo $3d_{5/2}$ XPS signal (Fig. 3a), this indicates that heating to 700 K for 30 min has resulted in dewetting of the 2.2 nm thick CSAF and the formation of structures with length scale on the order of 10 nm separated by darker regions that presumably expose the Mo substrate. The image in Fig. 4a is representative of those obtained from all regions of the CSAF with thickness < 4 nm after annealing at 700 K for 30 min. In contrast, the featureless micrograph (Fig. 4b) of the 5.2 nm thick region is representative of those from parts of the CSAF with initial thickness > 4 nm. The lack of contrast, coupled with the lack of Mo $3d_{5/2}$ XPS signal (Fig. 3) indicates that heating to 700 K for 30 min has not resulted in dewetting of the CSAF with initial thicknesses > 4 nm.

3.3. Thickness-dependent phases of Pd_zCu_{1-z} thin films

Mapping the Cu $2p_{3/2}$ CLS across Pd_zCu_{1-z} CSAFs has been used previously to map composition-dependent phase behavior in thick Pd_zCu_{1-z} and CuAuPd alloys [34,35]. Across a ~100 nm thick Pd_zCu_{1-z} CSAF annealed at 700 K, the Cu $2p_{3/2}$ CLS relative to that of pure Cu, $\Delta E_{CLS}{}^{Cu}(z) = E_{2p}{}^{Cu}(z) - E_{2p}{}^{Cu}(0)$, decreases monotonically with increasing z while the alloy is in the FCC phase. However there is an additional discontinuous CLS over the composition range $0.35 < z < 0.55$, in which the alloy adopts the B2 phase. Because XPS can detect signal from materials of < 1 nm thickness, the Cu $2p_{3/2}$ CLS is ideal for detecting the FCC-B2 phase transition in ultra-thin Pd_zCu_{1-z} alloy films; alloy morphologies whose phases can be difficult to determined using other methods.

The key result of this work is that XPS has shown that Pd_zCu_{1-z} films in the thickness range 4–6 nm do not exhibit the B2 phase observed in thicker films and in the bulk. In other words, for film thicknesses $d < 6$ nm the FCC phase of Pd_zCu_{1-z} with $0.35 < z < 0.55$ is dimensionally stabilized with respect to the B2 phase. Fig. 5a shows the Cu $2p_{3/2}$ CLS versus z at initial film thickness $d < 4$ nm, in the range $4 < d < 6$ nm and $d > 6$ nm after the Pd_zCu_{1-z} CSAF was annealed at 700 K. The additional CLS associated with the B2 phase is observed over the composition range $0.35 < z < 0.55$ for film thicknesses $d > 6$ nm [26,34]. When the film thickness falls in the range $4 < d < 6$ nm, the

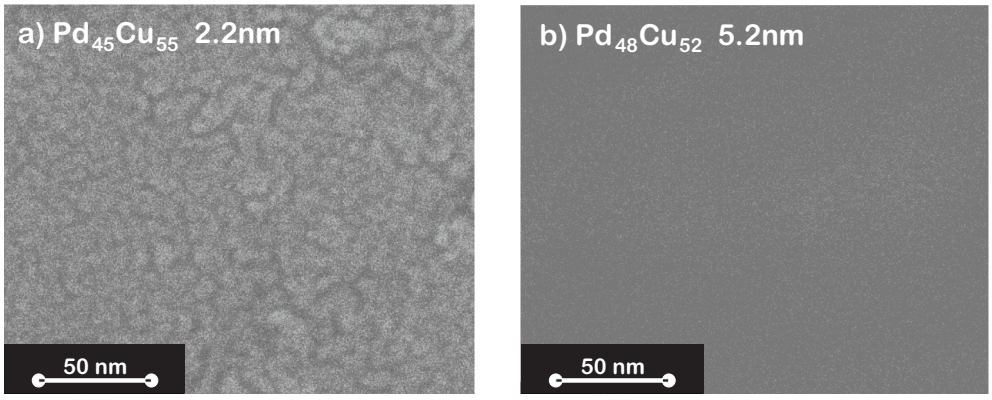

Fig. 4. SEM images (17.5 keV electron beam energy) of the Pd_zCu_{1-z} CSAF after annealing at 700 K for 30 min. (a) A dewetted region of the Pd_zCu_{1-z} CSAF with $z = 0.45$ and an initial thickness of $d = 2.2$ nm. (b) A region of continuous Pd_zCu_{1-z} film with $z = 0.48$ and an initial thickness of $d = 5.2$ nm.

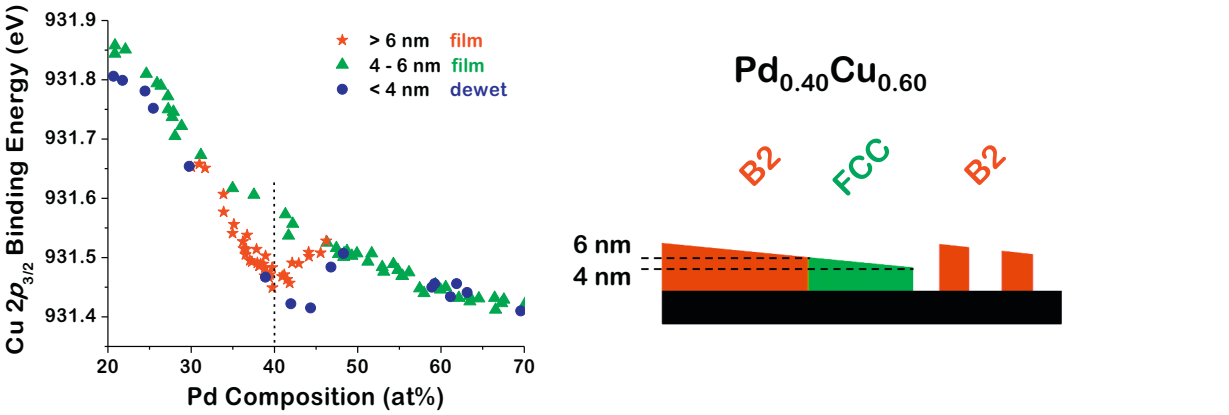

Fig. 5. a) Cu $2p_{3/2}$ binding energy measured versus Pd (at.%) after annealing the CSAF at 700 K for 30 min. Binding energies are grouped by film thickness: < 4 nm, 4–6 nm, and > 6 nm. b) Illustration of the thickness dependent phase behavior for $Pd_{0.40}Cu_{0.60}$. Films that are < 4 nm have dewetted and the Cu $2p_{3/2}$ peak exhibits the discontinuous CLS with composition that is indicative of the B2 phase. In the range 4–6 nm the CLS is absent, indicative of the FCC phase at all compositions. At > 6 nm the CLS associated with the B2 phase is evident.

Cu $2p_{3/2}$ binding energy decreases monotonically with increasing z, exhibiting no discontinuity over the composition range $0.35 < z < 0.55$ and indicating the presence of only the FCC phase. This result is consistent with prior measurements and simulations of Cu $2p_{3/2}$ CLS on bulk Pd_zCu_{1-z} samples annealed at 1000 K such that they adopted the FCC phase across the entire distribution range [41]. Note that at these thicknesses, the Pd_zCu_{1-z} CSAFs are continuous films and stable against dewetting.

An additional feature of our XPS data is that it indicates that for film morphologies generated by dewetting, the B2 phase is restabilized for compositions in the range $0.35 < z < 0.55$. Fig. 5a reveals that the CLS associated with the B2 phase over the composition range $0.35 < z < 0.55$ reappears at a film thickness < 4 nm, the thickness below which the Mo $3d_{5/2}$ XPS signal reveals that the Pd_zCu_{1-z} CSAF has dewetted from the Mo substrate. It is likely that dewetting allows the film to thicken locally to $d > 6$ nm, at which the B2 phase is still stable (Fig. 5b).

4. Discussion

The question to be addressed is the source of the energetic stabilization of the FCC phase over the B2 phase as the thickness of the film decreases to $d < 6$ nm. For a given phase of the film, the surface energy per unit area is independent of film thickness, however, the contribution of the bulk energy per unit area of the film decreases linearly with thickness. The bulk lattice parameter of the BCC phase of $Pd_{0.5}Cu_{0.5}$ is 0.301 nm, corresponding to a density of 73 atoms/nm^3 [42,43]. The lattice parameters for Cu and Pd in their FCC phases are 0.362 nm and 0.389 nm, respectively. Vegard's law predicts a lattice parameter of 0.375 for $Pd_{0.5}Cu_{0.5}$ in the FCC phase, corresponding to a density of 75 atoms/nm^3; almost identical to that of the B2 phase. Computational simulations of $Pd_{0.5}Cu_{0.5}$ in the FCC phase estimate a slightly lower density of 72 atoms/nm^3 [42,43]. In other words, all indications are that the densities of $Pd_{0.5}Cu_{0.5}$ in the FCC or the bulk equilibrium B2 phase do not differ significantly and, therefore, that in thin films a transition between the two phases would result in only a ~1% change of film thickness.

Recent Density Functional Theory simulations of bulk $Pd_{0.5}Cu_{0.5}$ in the FCC and B2 phases indicate that the B2 phase is stabilized by 1.9 kJ/mol·atom relative to the FCC phase. The observed phase transition can be rationalized, if the surface energy of the FCC phase is lower than that of the B2 phase. Given that the packing densities of the FCC surfaces are higher than those of the B2 phase, this seems like a reasonable assumption. Given that the densities of the FCC phase and the B2 phase of $Pd_{0.5}Cu_{0.5}$ are both ~73 atoms/nm^3, the difference in the bulk energies of a 6 nm thick films in the B2 and FCC phases is 1.2 J/m^2. This implies that in thin film and at 6 nm thickness the FCC phase will become stabilized relative to the B2 phase, if the FCC surface energy is 1.2 J/m^2 less than that of the B2 phase.

The surface energies of $Pd_{0.5}Cu_{0.5}$ in its B2 and FCC phases are not known, to our knowledge. One point of comparison for discussion of the role of surface energy in the stabilization of the FCC phase of $Pd_{0.5}Cu_{0.5}$ in thin film form are the surface energies of the different crystal phases of pure metals. These have been estimated using density function theory methods and tabulated recently in the Crystalium database [44]. The close-packed (111) surfaces of Cu and Pd have surface energies of 1.31 J/m^2 and 1.34 J/m^2, respectively. Of the low Miller index FCC surfaces, the (110) plane is the least densely packed and for Cu and Pd these have energies of 1.56 J/m^2 and 1.59 J/m^2, respectively. In these cases, the packing density reduces the surface energy by 0.25 J/m^2. This estimate of the potential contribution of surface energy to stabilization of the FCC phase of $Pd_{0.5}Cu_{0.5}$ in thin film form comes up short of the 1.2 J/m^2 that is estimated on the basis of density functional theory estimates of the bulk energies. However, it does demonstrate that the surface energy is in the right order of magnitude to contribute significantly to the dimensional stabilization of the FCC phase of $Pd_{0.5}Cu_{0.5}$.

5. Conclusion

High-throughput synthesis and characterization methodologies were implemented to determine the phase behavior of Pd_zCu_{1-z} alloy films spanning both composition and thickness. This approach has served to demonstrate the value of the XPS CLS as a means to explore the dimensional dependence of alloy phase diagrams and to identify a dimensionally stabilized phase of Pd_zCu_{1-z}. Alloy phases are most commonly determined using x-ray diffraction (XRD) or HR-TEM. XRD is difficult to perform on thin films and nanoscale morphologies, but the XPS based CLS method applied in this work provides a tool that is well-suited to the nanoscale regime. Spatially resolved XPS mapping of the Cu $2p_{3/2}$ CLS has successfully differentiated the ordered B2 and random FCC phases found over various ranges of composition and film thickness. The Cu $2p_{3/2}$ CLS works to differentiate these phases because the FCC-B2-FCC phase transitions are order-disorder transitions that result in discontinuous changes in the number of Cu atoms in a Cu nearest neighbor shell. In particular, at a film thickness < 6 nm, the FCC phase is stabilized over the composition range, $0.35 < z < 0.55$, where the ordered B2 phase exists in bulk. We also observed that Pd_zCu_{1-z} CSAF dewets the Mo substrate at a thicknesses < 4 nm, resulting in a morphology with a local thickness > 6 nm and the reappearance of the B2

phase in the composition region $0.35 < z < 0.55$. These results reveal an interplay between phase change (FCC-B2) and morphology change (dewetting) in response to reduction in Pd_zCu_{1-z} film thickness. They suggest that sufficiently small Pd_zCu_{1-z} alloy NPs would have an FCC structure over the composition range $0.35 < z < 0.55$.

Acknowledgements

The work presented herein has been support by the US National Science Foundation under grant number CHE1566228.

References

[1] A.E. Baber, H.L. Tierney, E.C.H. Sykes, Atomic-scale geometry and electronic structure of catalytically important Pd/Au alloys, ACS Nano 4 (2010) 1637–1645.
[2] J.M. Nam, C.S. Thaxton, C.A. Mirkin, Nanoparticle-based bio-bar codes for the ultrasensitive detection of proteins, Science 301 (2003) 1884–1886.
[3] Y. Lee, K. Koh, H. Na, K. Kim, J.J. Kang, J. Kim, Lithography-free fabrication of large area subwavelength antireflection structures using thermally dewetted Pt/Pd alloy etch Mask, Nanoscale Res. Lett. 4 (2009) 364–370.
[4] W. Juszczyk, Z. Karpinski, D. Lomot, J. Pielaszek, J.W. Sobczak, Pd-Au/SiO2 - characterization and catalytic activity, J. Catal. 151 (1995) 67–76.
[5] G.A. Somorjai, H. Frei, J.Y. Park, Advancing the frontiers in nanocatalysis, biointerfaces, and renewable energy conversion by innovations of surface techniques, J. Am. Chem. Soc. 131 (2009) 16589–16605.
[6] J. Wanjala, B. Luo, D. Fang, C.J. Zhong Mott, Gold-platinum nanoparticles: alloying and phase segregation, J. Mater. Chem. 21 (2011) 4012–4020.
[7] S. Srivastava, K.D. Chithra, S.K. Malviya, K. Chattopadhyay Sinha, Size dependent microstructure for Ag-Ni nanoparticles, Acta Mater. 59 (2011) 6501–6509.
[8] H. Yang Peng, Ag-Pt alloy nanoparticles with the compositions in the miscibility gap, J. Solid State Chem. 181 (2008) 1546–1551.
[9] H. Okamoto, T.B. Massalski, The Au－Pt (Gold-Platinum) system, Bull. Alloy Phase Diagr. 6 (1985) 46–56.
[10] S. Guerin, B.E. Hayden, D. Pletcher, M.E. Rendall, J.-P. Suchsland, Combinatorial approach to the study of particle size effects in electrocatalysis: synthesis of supported gold nanoparticles, J. Comb. Chem. 8 (2006) 791–798.
[11] R. Potyrailo, K. Rajan, K. Stoewe, I. Takeuchi, B. Chisholm, H. Lam, Combinatorial and high-throughput screening of materials libraries: review of state of the art, ACS Comb. Sci. 13 (2011) 579–633.
[12] W.F. Maier, K. Stowe, S. Sieg, Combinatorial and high-throughput materials science, Angew. Chem. Int. Ed. 46 (2007) 6016–6067.
[13] D. Farrusseng, High-throughput heterogeneous catalysis, Surf. Sci. Rep. 63 (2008) 487–513.
[14] J.R. Kitchin, A.J. Gellman, High-throughput methods using composition and structure spread libraries, AICHE J. 62 (2016) 3826–3835.
[15] S. Guerin, B.E. Hayden, D.C.A. Smith, High-throughput synthesis and screening of hydrogen-storage alloys, J. Comb. Chem. 10 (2008) 37–43.
[16] G. Gumuslu, P. Kondratyuk, J.R. Boes, B. Morreale, J.B. Miller, J.R. Kitchin, A.J. Gellman, Correlation of electronic structure with catalytic activity: H_2–D_2 exchange across Cu_xPd_{1-x} composition space, ACS Catal. 5 (2015) 3137–3147.
[17] S. Guerin, B.E. Hayden, C.E. Lee, C. Mormiche, A.E. Russell, High-throughput synthesis and screening of ternary metal alloys for electrocatalysis, J. Phys. Chem. B 110 (2006) 14355–14362.
[18] S. Yun, S.T. Oyama, Correlations in palladium membranes for hydrogen separation: a review, J. Membr. Sci. 375 (2011) 28–45.
[19] E.J. Granite, C.R. Myers, W.P. King, D.C. Stanko, H.W. Pennline, Sorbents for mercury capture from fuel gas with application to gasification systems, Ind. Eng. Chem. Res. 45 (2006) 4844–4848.
[20] K.J. Uffalussy, J.B. Miller, B.H. Howard, D.C. Stanko, C.R. Yin, E.J. Granite, Arsenic adsorption on copper-palladium alloy films, Ind. Eng. Chem. Res. 53 (2014) 7821–7827.
[21] H. Pennline, E. Granite, Sorbents for gasification processes, in: H. Pennline, E. Granite (Eds.), Mercury Control for Coal-Derived Gas Streams, Wiley-VCH Publ, 2015, pp. 357–374.
[22] A.M. Tarditi, C. Imhoff, F. Braun, J.B. Miller, A.J. Gellman, L. Cornaglia, PdCuAu ternary alloy membranes: hydrogen permeation properties in the presence of H2S, J. Membr. Sci. 479 (2015) 246–255.
[23] B.C. Nielsen, O.N. Dogan, B.H. Howard, E. Nall, Comparison of the corrosion of Cu50Pd50 and Cu50Pd44M6 (M = Y, Mg, or Al) hydrogen separation membrane alloys in simulated syngas containing H2S, Corros. Sci. 76 (2013) 170–181.
[24] J.B. Miller, D. Priyadarshini, A.J. Gellman, Segregation at the surfaces of CuxPd1-x alloys in the presence of adsorbed S, Surf. Sci. 606 (2012) 1520–1526.
[25] F. Braun, J.B. Miller, A.J. Gellman, A.M. Tarditi, B. Fleutot, P. Kondratyuk, L.M. Cornaglia, PdAgAu alloy with high resistance to corrosion by H_2S, Int. J. Hydrog. Energy 37 (2012) 18547–18555.
[26] D. Priyadarshini, P. Kondratyuk, Y.N. Picard, B.D. Morreale, A.J. Gellman, J.B. Miller, High-throughput characterization of surface segregation in CuxPd1-x alloys, J. Phys. Chem. C 115 (2011) 10155–10163.
[27] C.P. O'Brien, B.H. Howard, J.B. Miller, B.D. Morreale, A.J. Gellman, Inhibition of hydrogen transport through Pd and Pd47Cu53 membranes by H2S at 350 degrees C, J. Membr. Sci. 349 (2010) 380–384.
[28] J.B. Miller, C. Matranga, A.J. Gellman, Surface segregation in a polycrystalline $Pd_{70}Cu_{30}$ alloy hydrogen purification membrane, Surf. Sci. 602 (2008) 375–382.
[29] P. Kamakoti, D.S. Sholl, A comparison of hydrogen diffusivities in Pd and CuPd alloys using density functional theory, J. Membr. Sci. 225 (2003) 145–154.
[30] P.R. Subramanian, D.E. Laughlin, Cu-Pd (Copper-Palladium), J. Phase Equilib. 12 (1991) 231–243.
[31] P. Kamakoti, B.D. Morreale, M.V. Ciocco, B.H. Howard, R.P. Killmeyer, A.V. Cugini, D.S. Sholl, Prediction of hydrogen flux through sulfur-tolerant binary alloy membranes, Science 307 (2005) 569–573.
[32] Z.W. Dunbar, D. Chu, Thin palladium membranes supported on microstructured nickel for purification of reformate gases, J. Power Sources 217 (2012) 47–53.
[33] C.P. O'Brien, J.B. Miller, B.D. Morreale, A.J. Gellman, The kinetics of H_2–D_2 exchange over Pd, Cu, and PdCu surfaces, J. Phys. Chem. C 115 (2011) 24221–24230.
[34] J.R. Boes, P. Kondratyuk, C.R. Yin, J.B. Miller, A.J. Gellman, J.R. Kitchin, Core level shifts in Cu-Pd alloys as a function of bulk composition and structure, Surf. Sci. 640 (2015) 127–132.
[35] C. Yin, J.B. Miller, P. Kondratyuk, A.J. Gellman, Detection of CuAuPd phase boundaries using core level shifts, J. Phys. Chem. B 122 (2) (2018) 764–769.
[36] B. Fleutot, J.B. Miller, A.J. Gellman, Apparatus for deposition of composition spread alloy films: the rotatable shadow mask, J. Vac. Sci. Technol. A 30 (2012) 10.
[37] J.W. He, D.W. Goodman, D.G. Naugle, D.L. Cocke, Growth and interdiffusion of ultrathin films of Ti and Ni on Mo(110), Mater. Lett. 10 (1990) 250–255.
[38] M.A. Payne, J.B. Miller, A.J. Gellman, High-throughput characterization of early oxidation across $Al_xFe_yNi_{1-x-y}$ composition space, Corros. Sci. 91 (2015) 46–57.
[39] J.C. Russ, Energy dispersive spectrometers, Chapter 3, in: J.C. Russ (Ed.), Fundamentals of Energy Dispersive X-Ray Analysis, Butterworth-Heinemann, 1984, pp. 17–41.
[40] C.V. Thompson, Solid-state dewetting of thin films, Annu. Rev. Mater. Res. 42 (2012) 399–434.
[41] W. Olovsson, I.A. Abrikosov, B. Johansson, Core level shift in random CuPd and AgPd alloys by the complete screening picture, J. Electron Spectrosc. Relat. Phenom. 127 (2002) 65–69.
[42] J. Teeriniemi, P. Taskinen, K. Laasonen, First-principles investigation of the Cu-Ni, Cu-Pd, and Ni-Pd binary alloy systems, Intermetallics 57 (2015) 41–50.
[43] F.Y. Geng, J.R. Boes, J.R. Kitchin, First-principles study of the Cu-Pd phase diagram, Calphad-Comput. Coupl. Ph. Diag. Thermochem. 56 (2017) 224–229.
[44] R. Tran, Z.H. Xu, B. Radhakrishnan, D. Winston, W.H. Sun, K.A. Persson, S.P. Ong, Surface energies of elemental crystals, Sci. Data 3 (2016) UNSP 160080.